

GALAXIES PROBING GALAXIES AT HIGH RESOLUTION: CO-ROTATING GAS ASSOCIATED WITH A MILKY WAY ANALOG AT Z=0.4

ALEKSANDAR M. DIAMOND-STANIC^{1,2}, ALISON L. COIL³, JOHN MOUSTAKAS⁴, CHRISTY A. TREMONTI¹, PAUL H. SELL⁵,
ALEXANDER J. MENDEZ⁶, RYAN C. HICKOX⁷, & GREG H. RUDNICK⁸

Submitted to ApJ

ABSTRACT

We present results on gas flows in the halo of a Milky Way-like galaxy at $z = 0.413$ based on high-resolution spectroscopy of a background galaxy. This is the first study of circumgalactic gas at high spectral resolution towards an extended background source (i.e., a galaxy rather than a quasar). Using longslit spectroscopy of the foreground galaxy, we observe spatially extended H α emission with circular rotation velocity $v_{\text{circ}} \approx 270 \text{ km s}^{-1}$. Using echelle spectroscopy of the background galaxy, we detect Mg II and Fe II absorption lines at impact parameter $\rho = 27 \text{ kpc}$ that are blueshifted from systemic in the sense of the foreground galaxy's rotation. The strongest absorber ($\text{EW}_{2796} = 0.90 \text{ \AA}$) has an estimated column density ($N_H \geq 10^{19} \text{ cm}^{-2}$) and line-of-sight velocity dispersion ($\sigma = 17 \text{ km s}^{-1}$) that are consistent with the observed properties of extended H I disks in the local universe. Our analysis of the rotation curve also suggests that this $r \approx 30 \text{ kpc}$ gaseous disk is warped with respect to the stellar disk. In addition, we detect two weak Mg II absorbers in the halo with small velocity dispersions ($\sigma < 10 \text{ km s}^{-1}$). While the exact geometry is unclear, one component is consistent with an extraplanar gas cloud near the disk-halo interface that is co-rotating with the disk, and the other is consistent with a tidal feature similar to the Magellanic Stream. We can place lower limits on the cloud sizes ($l > 0.4 \text{ kpc}$) for these absorbers given the extended nature of the background source. We discuss the implications of these results for models of the geometry and kinematics of gas in the circumgalactic medium.

Subject headings: galaxies: evolution – galaxies: halos – galaxies: ISM

1. INTRODUCTION

The interplay between inflows and outflows of gas around galaxies has wide-ranging implications for galaxy evolution. Of particular interest are the roles of gas inflows and gas cooling for fueling the growth of galaxies (e.g., White & Rees 1978; White & Frenk 1991; Kereš et al. 2005; Dekel & Birnboim 2006; van de Voort et al. 2011; Faucher-Giguère et al. 2011) and the need to suppress star formation with feedback from massive stars and supermassive black holes to explain the observed galaxy luminosity function and color bimodality (e.g., Benson et al. 2003; Croton et al. 2006; Oppenheimer et al. 2010; Gabor et al. 2011; Vogelsberger et al. 2013; Hopkins et al. 2014). The accretion of gas onto dark matter halos is well understood in the context of our Λ CDM paradigm, but the kinematics and multi-phase structure of gas within halos are not uniquely predicted (e.g., Springel & Hernquist 2002; Agertz et al. 2007; Kaufmann et al. 2009; Kereš et al. 2009; Joung et al. 2012; Nelson et

al. 2013). This is an important problem, and its solution requires knowledge of both the accretion and feedback processes that regulate the efficiency with which halos convert their baryons into stars ($\Omega_*/\Omega_b \approx 5\%$; e.g., Bell et al. 2003; Moustakas et al. 2013; Planck Collaboration et al. 2013).

Cool gas clouds ($T \sim 10^4 \text{ K}$) in galaxy halos are of particular interest because they provide a source of fuel for subsequent star formation (e.g., Kereš & Hernquist 2009; Putman et al. 2012). They also play an important role in the acquisition of angular momentum for galaxy disks (e.g., Pichon et al. 2011; Stewart et al. 2013). These clouds can originate from cool inflows along filaments (e.g., Fumagalli et al. 2011; Stewart et al. 2011b), galactic winds (e.g., Heckman et al. 2000; Veilleux et al. 2005), accretion of gas previously ejected in a wind (e.g., Bregman 1980; Ford et al. 2014), thermal instabilities in a hot halo (e.g., Mo & Miralda-Escude 1996; Maller & Bullock 2004), and tidal interactions (e.g., Yun 1999; Besla et al. 2012).

Observations of Mg II $\lambda\lambda 2796, 2803$ absorption-line systems are useful for characterizing the cool gas in galaxy halos (e.g., Bergeron & Boissé 1991; Steidel et al. 1994; Churchill et al. 1996). Studies based on large samples of Mg II absorbers ($N \sim 10^3$) have used continuum and line emission (e.g., Zibetti et al. 2007; Ménard et al. 2011) and clustering (e.g., Bouché et al. 2006; Lundgren et al. 2009; Gauthier et al. 2009) to establish a general trend that stronger absorbers are more likely to be associated with star-forming galaxies. These trends with color or specific star-formation rate are not as obvious in moderately sized samples ($N \sim 10^2$) that associate

¹Department of Astronomy, University of Wisconsin-Madison, Madison, WI 53706, USA

²Grainger Fellow; aleks@astro.wisc.edu

³Center for Astrophysics and Space Sciences, University of California, San Diego, La Jolla, CA 92093, USA

⁴Department of Physics and Astronomy, Siena College, Loudonville, NY 12211, USA

⁵Department of Physics, Texas Tech University, Lubbock, TX 79409, USA

⁶Department of Physics and Astronomy, Johns Hopkins University, Baltimore, MD 21218, USA

⁷Department of Physics and Astronomy, Dartmouth College, Hanover, NH 03755, USA

⁸Department of Physics and Astronomy, University of Kansas, Lawrence, KS 66045, USA

individual Mg II absorbers with individual galaxies (e.g., Chen et al. 2010b; Nielsen et al. 2013), but it is clear that the average equivalent width and covering fraction are larger at smaller impact parameters. In particular, Mg II halos extend to $\rho \approx 100$ kpc for L^* galaxies with a covering fraction of $\approx 50\%$ for absorbers with $W_r(2796) \geq 0.5 \text{ \AA}$ (Chen et al. 2010a), and the covering fraction at $\rho < 25$ kpc approaches unity (e.g., Kacprzak et al. 2013).

Beyond these trends with impact parameter, there is strong evidence that the equivalent width and covering fraction of Mg II absorbers depends on the orientation of the background sightline with respect to the disk of the foreground galaxy. For example, when stacking low-resolution spectra of $z_{\text{phot}} > 1$ galaxies behind $0.5 < z_{\text{spec}} < 0.9$ galaxies, Bordoloi et al. (2011) found that edge-on disk galaxies at small impact parameter ($\rho < 40$ kpc) exhibit three times stronger absorption along the minor axis than along the major axis. This is consistent with the signature of bipolar outflows driven perpendicular to the plane of the disk, as observed in local starburst galaxies (e.g., Bland & Tully 1988; Shopbell & Bland-Hawthorn 1998; Ohyama et al. 2002). It is also consistent with the incidence of outflowing gas traced by Mg II absorption in down-the-barrel sightlines towards star-forming galaxies, both for stacked spectra (e.g., Weiner et al. 2009; Rubin et al. 2010b) and for spectra of individual galaxies (e.g., Tremonti et al. 2007; Diamond-Stanic et al. 2012; Kornei et al. 2012; Erb et al. 2012; Martin et al. 2012; Rubin et al. 2014). This empirical evidence for winds perpendicular to the disk has motivated studies of the spatial extent, mass, and kinematics of outflowing gas for individual galaxies based on sightlines towards background quasars (e.g., Tripp et al. 2011; Bouché et al. 2012; Gauthier & Chen 2012; Lundgren et al. 2012).

In addition to a preference for absorption along the minor axis, there is evidence for Mg II absorption associated with the plane of the disk. In particular, Bouché et al. (2012) and Kacprzak et al. (2012) argued that the distribution of azimuthal angles for individual Mg II absorbers is bimodal, with gas being found preferentially within $\approx 20^\circ$ of either the minor or major axis. While it is challenging to characterize the detailed three-dimensional geometry of cool halo gas based on individual sightlines, there are clear examples for which Mg II absorbers are co-rotating with the stellar disk (e.g., Steidel et al. 2002; Chen et al. 2005; Kacprzak et al. 2010, 2011a; Bouché et al. 2013). For example, Steidel et al. (2002) compared the kinematics of Mg II absorbers at $\rho = 10\text{--}50$ kpc to emission-line rotation curves at $r \leq 10$ kpc and found that the absorption-line velocities were often offset from the systemic redshift in the sense of the galaxy’s rotation. In detail, the full velocity ranges of Mg II absorption ($\Delta v \approx 100\text{--}200 \text{ km s}^{-1}$) were broader than expectations for a single thick disk, but the overall kinematics were clearly dominated by rotation.

While absorption-line studies of halo gas have typically used sightlines to background quasars, the advent of large redshift surveys and sensitive spectroscopy with 8–10 m class telescopes has enabled the use of background galaxies as light beacons. This has been done in both stacked (e.g., Steidel et al. 2010; Bordoloi et al. 2011)

and individual spectra (e.g., Adelberger et al. 2005; Rubin et al. 2010a; Steidel et al. 2010) at low spectral resolution. Compared to background quasars, the extended light profiles of background galaxies provide an opportunity to study absorption over a larger solid angle through a given halo (e.g., Rubin et al. 2010a), and the number density of galaxies on the sky offers significantly more sightlines to study halo gas in absorption at faint magnitudes (e.g., Barger et al. 2008).

However, it has not yet been possible to obtain spectroscopic data for individual background galaxies that are of comparable quality (e.g., S/N, spectral resolution) to what is available for background quasars. In particular, high-resolution spectroscopy is required to measure the kinematics, column density, and covering fractions for individual absorption components, and these measurements provide important constraints for models of cool gas clouds in the circumgalactic medium.

In this paper, we use a bright galaxy from the Diamond-Stanic et al. (2012) sample as a background light source ($z_{bg} = 0.712$) to probe halo gas associated with a disk galaxy ($z_{fg} = 0.413$) at impact parameter $\rho = 27$ kpc. The brightness of the background galaxy ($g = 19.6$) offers the first opportunity to study halo gas at high spectral resolution towards an extended background source. We describe the data used in this study in Section 2. We present results on the properties of the foreground disk galaxy and its circumgalactic gas in Section 3 and 4. We discuss the implications of these results in Section 4, and we summarize our main conclusions in Section 5. Throughout the paper, we adopt a cosmology with $h = 0.7$, $\Omega_M = 0.3$, and $\Omega_\Lambda = 0.7$.

2. DATA

2.1. *HST/WFC3*

Observations with the Wide Field Camera 3 on the Hubble Space Telescope were obtained on 2010 Dec 15 as part of program 12272. As described by Diamond-Stanic et al. (2012), we obtained 4×10 min exposures in a single orbit using the F814W filter on the UVIS channel (pixel size $0.04''$), and we combined the dithered images to produce a science mosaic with $0.02''$ pixels. An $11'' \times 11''$ portion of the image including the foreground disk galaxy and the compact background galaxy is shown in Figure 1.

2.2. *Keck/LRIS*

Observations with the Low Resolution Imaging Spectrometer (LRIS, Oke et al. 1995) on the Keck I telescope were obtained on 2011 Mar 7. Using a $1''$ longslit and the D560 dichroic, we obtained a 30-min exposure with the 400/3400 grism on the blue side ($R \approx 600$) and 2×15 min exposures with the 400/8500 grating on the red side ($R \approx 1000$). The slit position angle was set to -41.9 deg to include both the background (SDSS J090523.59+575912.4) and foreground (SDSS J090524.08+575915.9) galaxies (see the solid red lines in Figure 1). The data were processed with the XIDL LowRedux⁹ pipeline.

2.3. *Keck/HIRES*

⁹ <http://www.ucolick.org/~xavier/LowRedux/>

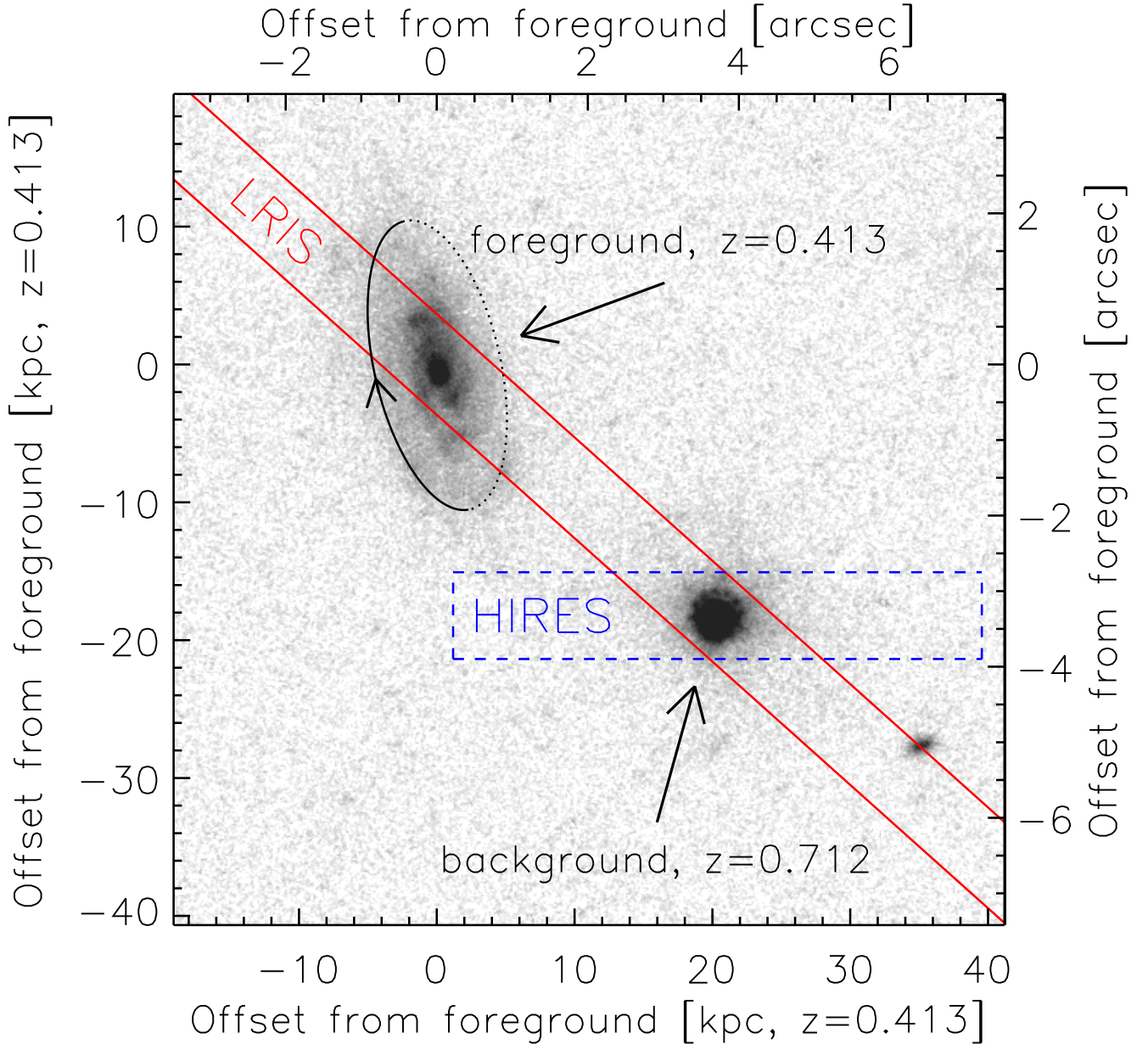


FIG. 1.— HST WFC3/UVIS F814W image of the background and foreground galaxies described in this paper. The positions and orientations of the Keck/LRIS (solid red lines) and Keck/HIRES (dashed blue rectangle) slits are shown. The orientation of the foreground disk is shown by an ellipse, and the direction of rotation is indicated by the arrow on the near side of the disk. The dotted portion of the ellipse corresponds to the far side of the disk, which is oriented into the page.

Observations of the background galaxy with the High Resolution Echelle Spectrometer (HIRES, Vogt et al. 1994) on the Keck I telescope were obtained on 2009 Dec 11. We obtained 2×1 hr exposures using the HIRESb configuration with a $1.148'' \times 7.0''$ slit (see the dashed blue rectangle in Figure 1), which provides a spectral resolution of $R \approx 37,000$ and a velocity resolution of 8 km s^{-1} . The data were processed with the XIDL HIRedux¹⁰ pipeline. The spectrum of the background galaxy is fairly smooth near the foreground absorption lines (Diamond-Stanic et al. 2012), and we fit the continuum for each order using a low-order polynomial, ex-

cluding regions of line absorption and emission. The continuum-normalized data from the two exposures and from overlapping regions between the orders were combined using an inverse-variance weighted mean.

2.4. *Spitzer/IRAC*

Observations with the Infrared Array Camera (IRAC, Fazio et al. 2004) on the Spitzer Space Telescope were obtained on 2009 Nov 27 as part of Program 60145. We obtained 5×30 sec dithered exposures in the $3.6 \mu\text{m}$ and $4.5 \mu\text{m}$ bands. We performed photometry on the post-basic calibrated using the MOPEX point-source extraction software (Makovoz & Marleau 2005). Given the close spatial separation of the background and fore-

¹⁰ <http://www.ucolick.org/~xavier/HIRedux/>

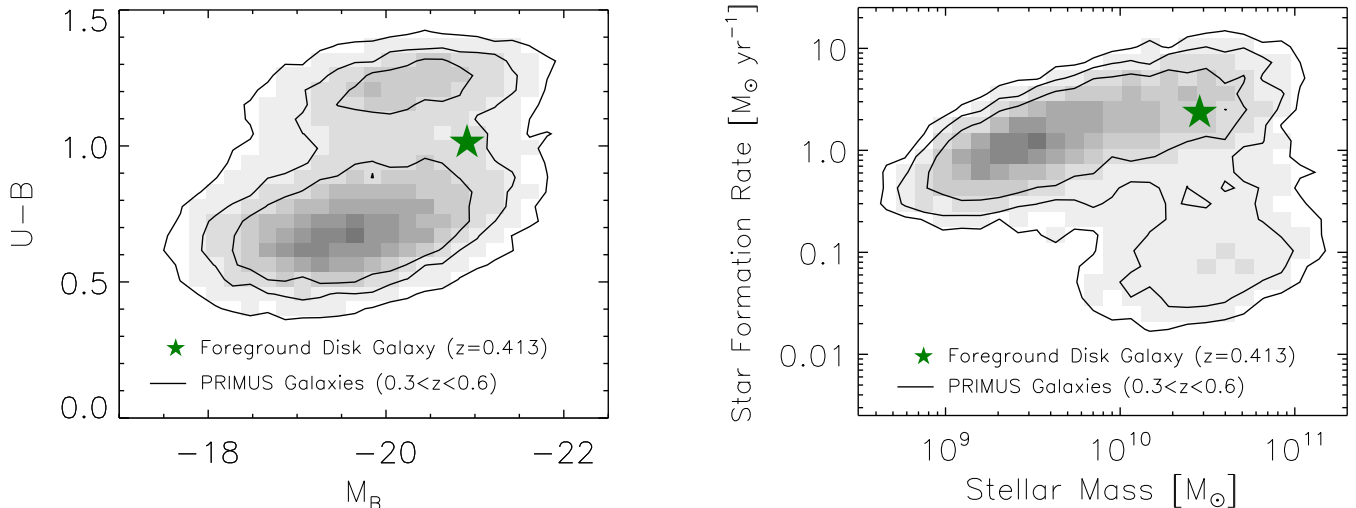


FIG. 2.— *Left*: This color-magnitude diagram shows the location of the foreground galaxy with respect to a comparison sample of $\approx 50,000$ galaxies at comparable redshifts from the PRIMUS survey. The contours encompass 50%, 75%, and 90% of the galaxies from the comparison sample. The $U - B$ color of the foreground galaxy place it near the luminous end of the green valley. *Right*: The star-formation rate vs stellar mass plane for the same set of galaxies, which illustrates the location of the foreground galaxy near the massive end of the star-forming sequence.

ground galaxies ($5.2''$) and the spatial resolution of IRAC (FWHM = $1.7''$), we used point-source photometry to properly deblend the two galaxies.

3. PROPERTIES OF THE FOREGROUND DISK GALAXY

3.1. Redshift, Rest-frame Color, Stellar Mass

We measure a systemic redshift of $z = 0.4134 \pm 0.0001$ for the foreground disk galaxy based on [O II] $\lambda 3727$, [O III] $\lambda 5007$, and H α $\lambda 6563$ emission lines in the Keck/LRIS spectrum. We then use K-correct (Blanton & Roweis 2007) to estimate rest-frame color ($U - B = 1.01$) and absolute magnitude ($M_B = -20.91$) based on photometry from the Sloan Digital Sky Survey (SDSS Abazajian et al. 2009) and from Spitzer/IRAC. We estimate the stellar mass ($M_* \approx 10^{10.46} M_\odot$) and star formation rate (SFR $\approx 2.4 M_\odot \text{ yr}^{-1}$) from the same photometry using iSEDfit, the spectral energy distribution modeling code described by Moustakas et al. (2013). These values are derived following the fiducial method from Moustakas et al. (2013), which uses Flexible Stellar Population Synthesis models (Conroy et al. 2009; Conroy & Gunn 2010), a Chabrier (2003) initial mass function from 0.1 to $100 M_\odot$, and the time-dependent dust attenuation curve of Charlot & Fall (2000).

We show the location of the foreground disk galaxy on a color-magnitude diagram and a star formation rate-stellar mass diagram in Figure 2. As a comparison sample, we include $\approx 50,000$ galaxies at $0.3 < z < 0.6$ from the Prism Multi-object Survey¹¹ (PRIMUS, Coil et al. 2011a; Cool et al. 2013; Moustakas et al. 2013). This figure illustrates that the foreground disk galaxy resides on the luminous end of the green valley (e.g., Mendez et al. 2011) and the massive end of the star-forming sequence (e.g., Noeske et al. 2007). The dust attenuation we estimate from iSEDfit is $A_V \approx 0.5$, which is consistent

with a star-forming galaxy viewed at moderate inclination. The stellar mass and luminosity of the foreground galaxy place it near M^* for the stellar mass function (Moustakas et al. 2013) and L^* for the luminosity function at $z \approx 0.4$ (Willmer et al. 2006). In particular, the foreground galaxy would be $(1.2, 1.1, 0.8) \times L^*$ as defined by the B -band luminosity function for (blue, red, all) galaxies at $z = 0.5$ from Willmer et al. (2006).

3.2. Rotation curve and dynamical mass

We show the two-dimensional Keck/LRIS spectrum in the region surrounding the H α emission line for the foreground galaxy in Figure 3. The H α emission is spatially extended and exhibits the signature of rotation with a line-of-sight amplitude $v_{los} = 178 \pm 10 \text{ km s}^{-1}$. We can convert this into a circular rotation velocity (v_{rot}) by accounting for the disk inclination (i) and the azimuthal angle of the slit relative to the major axis of the disk (α). Following Chen et al. (2005) and Chen et al. (2014), this conversion can be expressed in terms of i and α for any location in the disk plane.

$$\frac{v_{rot}}{v_{los}} = \frac{\sqrt{1 + \sin^2 \alpha \tan^2 i}}{\cos \alpha \sin i} \quad (1)$$

We fit an exponential profile to the HST data with GALFIT (Peng et al. 2002) to estimate the axis ratio ($b/a = 0.39$) and position angle of the disk (PA = 15.8°). This implies a disk inclination $i = 67^\circ$ and an azimuthal angle $\alpha = 33^\circ$ of the background sightline relative to the major axis of the foreground disk. Given the systematic uncertainties associated with estimating projection parameters for spiral galaxies (e.g., Barnes & Sellwood 2003), we adopt $\pm 5^\circ$ uncertainties on the inclination and azimuthal angles.

Before using equation 1 to estimate a circular velocity, we need to account for the fact that each spatial bin of the LRIS spectrum includes emission from regions that span a large range in azimuthal angle. For

¹¹ <http://primus.ucsd.edu/>

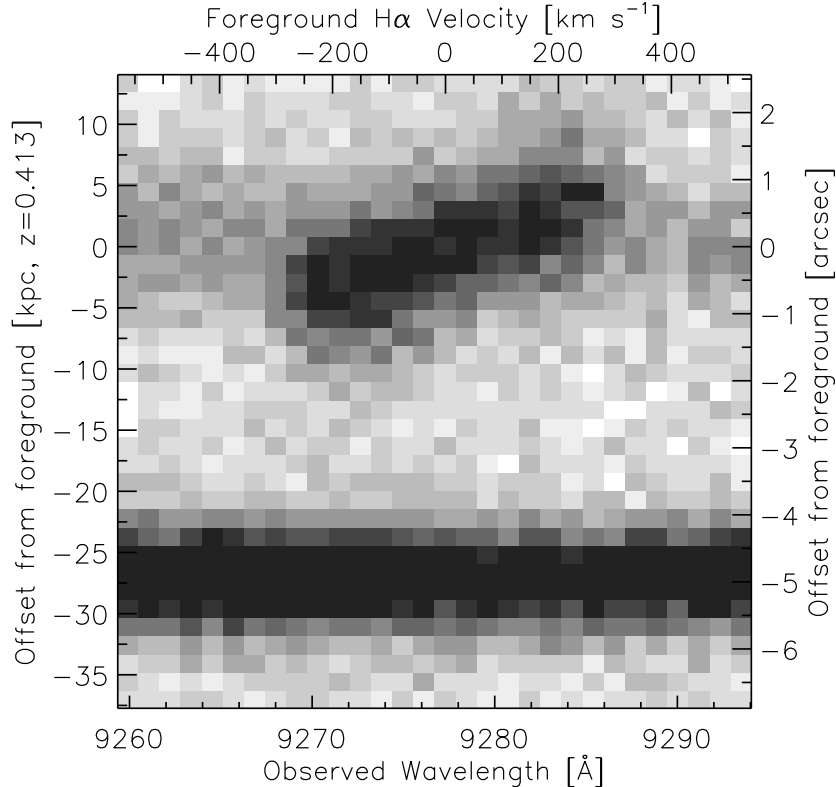


FIG. 3.— The two-dimensional spectrum from Keck/LRIS near $\lambda_{\text{obs}} = 9276 \text{ \AA}$, showing the H α emission from the foreground galaxy (top) and the bright continuum of the background galaxy (bottom). The H α emission from the foreground galaxy is spatially extended and exhibits the signature of rotation. The ionized gas in the disk of foreground galaxy is blueshifted by $v \approx -200 \text{ km s}^{-1}$ on the side closest to the background galaxy.

example, Figure 1 shows that the brightest regions of the galaxy that fall within the slit are close to the major axis (i.e., they have small α angles). To account for this, we determine all the locations in the galaxy that would fall in each $1.0''$ wide \times $0.2''$ long spatial bin along the LRIS slit. We calculate the relevant α angle for all 500 pixels in the bin and then determine the appropriate $v_{\text{rot}}/v_{\text{los}}$ ratio by computing a flux-weighted average, assuming that the H α morphology is similar to the observed HST morphology at $\lambda_{\text{rest}} \approx 5800 \text{ \AA}$. For the spatial bins that correspond to the flat part of the observed rotation curve, we find that this ratio converges to $v_{\text{rot}}/v_{\text{los}} = 1.51 \pm 0.05$, which corresponds to a circular rotation velocity $v_{\text{rot}} = 269 \pm 18 \text{ km s}^{-1}$.

The GALFIT profile fitting also yields an estimate of the half-light radius, $r_e = 5.7 \pm 0.3 \text{ kpc}$. We estimate the uncertainty in this value from variations between fits that include Sersic profiles (n is a free parameter) and exponential profiles ($n = 1$), and fits that include a second component to model emission from the central kiloparsec of the galaxy. For the two-component fits, the fainter central component contributes $7 \pm 2\%$ of the total light and has $r_e = 0.4 \pm 0.1 \text{ kpc}$. The best-fit Sersic index for this central component is $n = 0.6 \pm 0.1$, which indicates that it does not exhibit the characteristics of a classical bulge (i.e., it is not well fit by an $n = 4$ de Vaucouleurs profile).

We note that a circular velocity $v_c = 269 \text{ km s}^{-1}$ at $r_e = 5.7 \text{ kpc}$ corresponds to a dynamical mass $M_{\text{dyn}}(r <$

$r_e) \approx r_e v_c^2 / G = 9.6 \times 10^{10} \mathcal{M}_{\odot}$, which is 0.5 dex larger than our estimate of the stellar mass above. This offset is somewhat larger than the 0.3 dex systematic uncertainty in the stellar mass estimate, so this suggests that the dynamical mass has comparable contributions from baryons and dark matter within the effective radius.

4. PROPERTIES OF GAS IN THE CIRCUMGALACTIC MEDIUM

As discussed in the Introduction, the serendipitous superposition of the background and foreground galaxies on the plane of the sky presents an opportunity to study gas in the circumgalactic medium (CGM) of the foreground galaxy at impact parameter $\rho = 27 \text{ kpc}$. In particular, we are able to measure the column density and kinematics of gas in absorption along the line of sight to the background galaxy at high spectral resolution (FWHM $\approx 8 \text{ km s}^{-1}$). In this section, we present these measurements, and we describe the kinematic modeling that is necessary to interpret the observed line-of-sight velocities in terms of a rotating disk, a warped disk, or an outflowing wind.

4.1. Observed column densities and kinematics

We show the continuum-normalized Keck/HIRES data for the Mg II $\lambda\lambda 2796, 2803$ and Fe II $\lambda\lambda 2586, 2600$ absorption lines in Figure 4. We also use spectral coverage of three other Fe II lines (2344, 2374, 2382) in our analysis. We detect an optically thick absorption component cen-

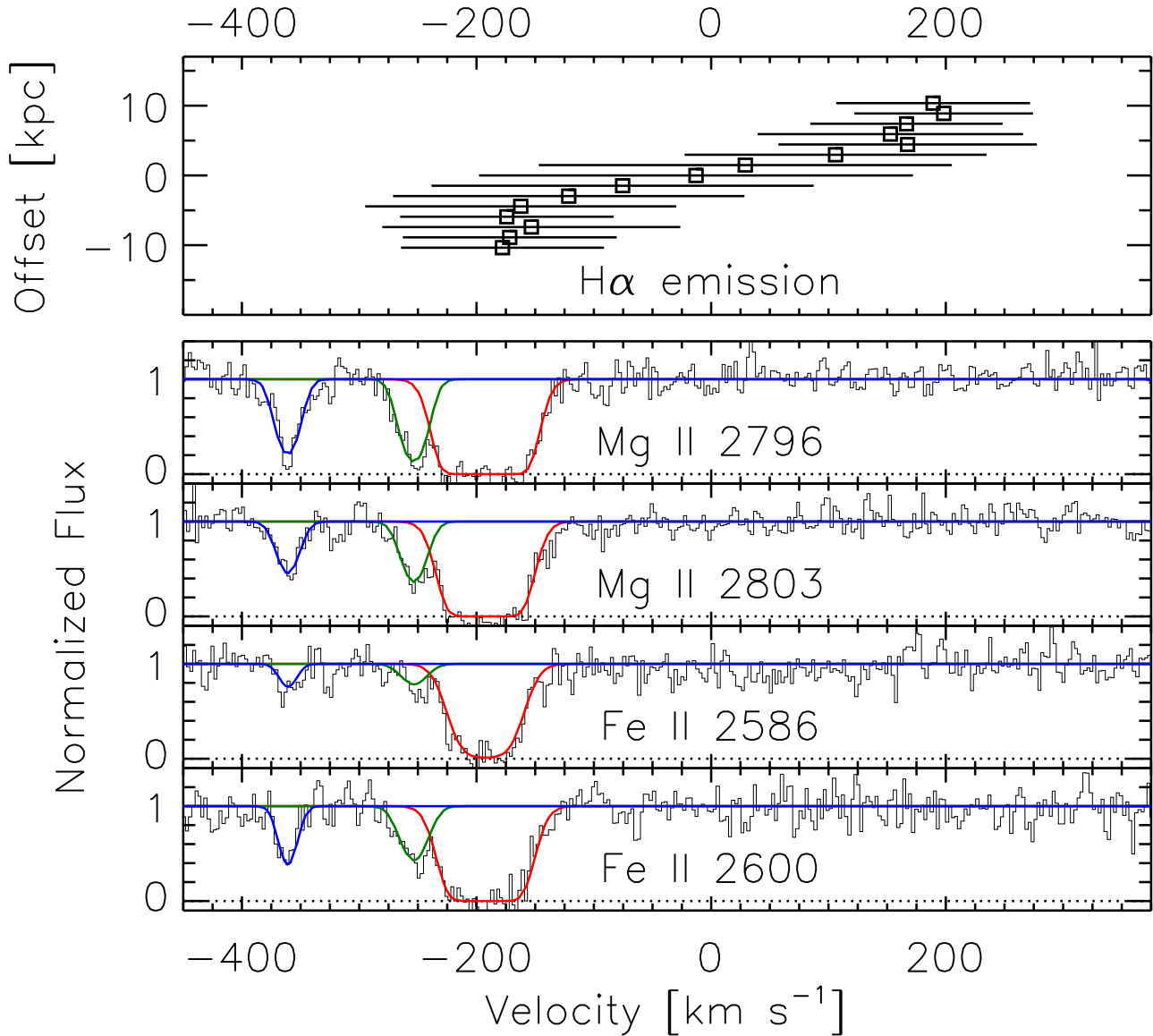


FIG. 4.— Continuum-normalized spectra from Keck/HIRES showing absorption-line profiles for four transitions associated with the foreground galaxy (Mg II 2796, 2803; Fe II 2586, 2600). The solid red, green, and blue curves in each panel show the best-fit Voigt profiles for three components at $v = -195 \text{ km s}^{-1}$, $v = -256 \text{ km s}^{-1}$, and $v = -363 \text{ km s}^{-1}$ relative to the systemic redshift of the foreground galaxy ($z = 0.4134$). The kinematics of the strongest component at $v = -195 \text{ km s}^{-1}$ suggest that it is consistent with an extension of a flat rotation curve to $r \approx 30 \text{ kpc}$.

tered near $v \approx -200 \text{ km s}^{-1}$, along with two weaker components near $v \approx -260 \text{ km s}^{-1}$ and $v \approx -360 \text{ km s}^{-1}$. We use VPFIT¹² to perform a joint fit to all three components for both ions to measure precise column densities and kinematics (see Figure 4 and Table 1). In particular, we require that the redshifts (i.e., centroid velocities) for the three velocity component be the same for both Mg II and Fe II but we allow the b values and column densities to be fit independently for each ion.

Using reasonable assumptions about gas-phase abundances and ionization, we can estimate the hydrogen column density and [Mg/Fe] for each velocity component. For our fiducial estimates, we assume no dust depletion

and solar metallicity, and we assume that Mg II and Fe II are the dominant tracers of Mg and Fe, respectively. Relaxing any of these assumptions would increase our estimates of N_H (i.e., dust depletion or lower metallicity would reduce the gas-phase abundance of Mg and Fe relative to hydrogen, and other ionization phases could contribute additional Mg and Fe). Based on the Fe II column densities, these fiducial assumptions imply hydrogen column densities $N_H \geq 1.2 \times 10^{19} \text{ cm}^{-2}$ for the strongest component and $N_H \geq 3\text{--}4 \times 10^{17} \text{ cm}^{-2}$ for the two weaker components. We note that the estimated dust depletion for Fe in the warm ionized medium is -0.8 dex (e.g., Jenkins 2009; Draine 2011) and Lyman Limit Systems are typically associated with sub-solar metallicity (e.g., Lehner et al. 2013), so these N_H values could be larger

¹² <http://www.ast.cam.ac.uk/rfc/vpfit.html>

by an order of magnitude.

Based on the Mg II and Fe II column densities, all three velocity components have $[\text{Mg}/\text{Fe}] \approx -0.2$. The Mg II lines for the strongest component are saturated, which implies that there could be contributions from unresolved velocity subcomponents. That said, the Fe II lines span a much wider range in optical depth, and the b values we measure for the Mg II and Fe II components are nearly identical. This suggests that our column density measurements for both ions are robust, even for this strongest component. We note that correcting for dust depletion would further decrease $[\text{Mg}/\text{Fe}]$ because Mg is less depleted than Fe (e.g., Jenkins 2009; Draine 2011). The small $[\text{Mg}/\text{Fe}]$ ratio for this absorbing gas suggests that it has been significantly enriched in Fe by previous generations of type 1a supernovae (e.g., Rigby et al. 2002).

4.2. Kinematics of gas in the disk plane

If the kinematics of these absorbers were dominated by disk rotation in the plane defined by the stellar emission, we could convert the observed line-of-sight velocities (v_{los}) into deprojected rotation velocities (v_{rot}). This depends on the sine of the disk inclination angle (i) and the cosine of the azimuthal angle in the plane of the disk (ϕ).

$$\frac{v_{rot}}{v_{los}} = \frac{1}{\sin i \cos \phi} \quad (2)$$

Following Steidel et al. (2002), the angle ϕ can be expressed in terms of the impact parameter measured along the major axis (p) and the distance along the minor axis where the line of sight intersects the disk plane (y_0).

$$\cos \phi = \frac{p}{\sqrt{p^2 + y_0^2}} = \frac{1}{\sqrt{1 + (y_0/p)^2}} \quad (3)$$

These values can be determined from the impact parameter (ρ) and the azimuthal angle in the plane of the sky (α).

$$p = \rho \cos \alpha ; y_0 = \frac{\rho \sin \alpha}{\cos i} \quad (4)$$

We note that substituting the values from equations 3 and 4 into equation 2 yields the expression in equation 1.

Based on the above, we find $v_{rot}/v_{los} = 2.1$, $p = 22$ kpc, $y_0 = 37$ kpc, $r = 43$ kpc, and $\phi = 59^\circ$. We mark this location with a red circle in Figure 5, which shows the projection of the disk on the plane of the sky along with $y-z$ (edge-on) and $x-y$ (face-on) views of the disk plane. The velocity ratio implies deprojected rotation velocities $v_{rot} = [-410, -540, -760]$ km s⁻¹ for the three absorption components. All of these values would be inconsistent with the Tully-Fisher relation (e.g., Tully & Fisher 1977; McGaugh et al. 2000) and the observed rotational velocity of the stellar disk (Section 3.2), which suggests that the absorbers are either not located in the disk plane defined by the stellar disk, or their kinematics are not dominated by rotation.

4.3. Kinematics of gas in a warped disk

Our line of sight would also intersect clouds located above and below the disk plane, and if the kinematics were dominated by rotation, the v_{rot}/v_{los} ratio would also be determined by equation 2. The relevant ϕ angle

would depend on the y coordinate along the minor axis, which can be calculated for any point along the line-of-sight vector \mathbf{L} by considering its projection along the y and z planes.

$$x = p ; y = y_0 - |\mathbf{L}| \sin i ; z = z_0 + |\mathbf{L}| \cos i \quad (5)$$

Here the x coordinate is measured along the major axis in the disk plane, the y coordinate is measured along the minor axis in the disk plane, and the z coordinate is measured along the vertical axis above the disk plane. For example, the reference position $y_0 = 37$ kpc corresponds to $z_0 = 0$ (i.e., crossing the disk plane), and a location $|\mathbf{L}| = 40$ kpc along the line of sight from this reference position would have $y = 0$ and $z = 16$ kpc (i.e., crossing the major axis of the disk). The y coordinate then determines v_{rot}/v_{los} for every point along the line of sight based on equations 2 and 3.

Therefore, we can determine the location that would yield an observed line-of-sight velocity for a given rotation velocity. If we use the rotation velocity of the stellar disk ($v_{rot} = 269$ km s⁻¹), the strongest absorber could be at $|\mathbf{L}| = 21$ kpc ($z = 8$ kpc, $r = 30$ kpc, $v_{rot}/v_{los} = 1.4$), which is marked by a red star in Figure 5. If this location were associated with a warped disk, the relevant warp angle would be $\tan^{-1} z/r = 16^\circ$.

4.4. Kinematics associated with outflowing gas

If the kinematics of the absorbers were dominated by an outflowing wind, we could convert the observed line-of-sight velocities into three-dimensional wind velocities. The ratio of the wind velocity (v_w) to the line-of-sight velocity (v_{los}) can be expressed in terms of the angle (i_w) between the wind vector and the line of sight.

$$\frac{v_w}{v_{los}} = \frac{1}{\cos i_w} \quad (6)$$

For a wind vector that is orthogonal to the disk plane (i.e., along the z axis) the angle i_w would be equal to the disk inclination angle (i). More generally, the angle i_w can be expressed in terms of the length of the wind vector (r_w) and its projection on the plane of the sky (i.e., the impact parameter, ρ).

$$\sin i_w = \frac{\rho}{r_w} \quad (7)$$

Following Gauthier & Chen (2012), r_w can be expressed in terms of the z height above the disk plane and the half opening angle of the wind with respect to the z axis (θ_w).

$$r_w = \frac{z}{\cos \theta_w} \quad (8)$$

Thus for any location along the line of sight (equation 5), we can calculate the galactocentric radius (r_w), the opening angle of a wind vector that intersects the line of sight (θ_w), and the associated v_w/v_{los} ratio.

We can therefore determine the minimum opening angle required to intersect the line of sight and the maximum opening angle beyond which one would expect a broader range of line-of-sight velocities than is observed. The minimum opening angle $\theta_w = 51^\circ$ corresponds to $|\mathbf{L}| = 55$ kpc ($z = 21$ kpc, $v_w/v_{los} = 1.6$), and we

mark this location with a red triangle in Figure 5. For an outflow with an opening angle $\theta_w > 51^\circ$, the line of sight would enter (exit) the outflow cone at some lower (higher) z height for which a smaller (larger) fraction of its velocity would be along the line of sight (e.g., Gauthier & Chen 2012). For example, an outflow with $\theta_w = 52^\circ$ would span a range $|\mathbf{L}| = 46\text{--}68$ kpc ($z = 18\text{--}26$ kpc) and exhibit v_w/v_{los} values that vary by a factor of 1.9, which matches to the range of absorption-line velocities we observe. Therefore, in the context of a conical outflow model, larger opening angles $\theta_w > 52^\circ$ can be ruled out because they would be associated with an even broader range of line-of-sight velocities than we observe. We note that an outflow model with $\theta_w > 60^\circ$ would also be associated with redshifted components, and a model with $\theta_w > 67^\circ$ would additionally produce a blueshifted “down-the-barrel” component in self-absorption towards the foreground galaxy, neither of which is observed.

5. DISCUSSION

We have presented results on a Milky-Way-like disk galaxy at $z = 0.4$, including the column density and kinematics of its circumgalactic gas as traced by Mg II and Fe II absorption lines at impact parameter $\rho = 27$ kpc. The CGM absorption lines are blueshifted in the sense of the galaxy’s rotation, and here we evaluate the hypothesis that this gas is associated with an extended, warped gaseous disk. We also consider whether some components of this absorption could be associated extraplanar halo gas. This interpretation is relevant because an extended disk may trace recent accretion of gas from the intergalactic medium (e.g., Ostriker & Binney 1989; Stewart et al. 2013), and extraplanar halo gas may trace outflows or gas recycling in a galactic fountain (e.g., Shapiro & Field 1976; Bregman 1980; Ford et al. 2014). We also discuss the size constraints that can be placed on the absorbing clouds due to the extended size of the background source. We present this discussion in the context of previous observations of gas around galaxies as traced by emission and absorption, and we compare to expectations from simulations of gas in the circumgalactic medium.

5.1. Evidence for an extended, warped disk

In the local universe, extended H I disks have been observed in emission around disk galaxies with spatial extents $r_{\text{HI}} = 10\text{--}50$ kpc for mass surface densities $\Sigma_{\text{HI}} = 1 \mathcal{M}_\odot \text{pc}^{-2}$ ($N_{\text{H}} \approx 10^{20} \text{cm}^{-2}$); this spatial extent is a function of H I mass such that galaxies with $M_{\text{HI}} > 10^{10} \mathcal{M}_\odot$ generally have $r_{\text{HI}} > 30$ kpc (e.g., Broeils & Rhee 1997). Most of these H I disks exhibit warps beyond the optical extent of the disk (e.g., Sancisi 1976; Bosma 1991; Sancisi et al. 2008), and the angles of these warps with respect to the stellar disk can be as large as $20^\circ\text{--}30^\circ$ (e.g., García-Ruiz et al. 2002). In terms of kinematics, these warped disks are also dynamically thin, with typical velocity dispersions $\approx 10 \text{km s}^{-1}$ (e.g., Bosma 1991; Bottenga 1996). There are several explanations for the physical origin of warps, including interactions with nearby dwarf galaxies (e.g., Shang et al. 1998) and cosmic infall of gas with misaligned angular momentum (e.g., Ostriker & Binney 1989; Jiang & Binney 1999; Shen & Sellwood 2006).

In the context of this paper, an extended disk provides a straightforward explanation for the optically thick absorption component at $v_{los} = -195 \text{km s}^{-1}$. Given the incidence of extended disks around massive, star-forming galaxies in the local universe, it is reasonable to expect that our line of sight would intersect an extended disk. Galaxies at $z = 0.4$ also tend to have higher gas fractions than galaxies at $z = 0$ (e.g., Rao et al. 2006; Combes et al. 2013), which provides additional support for this interpretation. Furthermore, the estimated H I column density is consistent with the expected surface density of an extended disk, and the kinematics agree with a flat rotation curve ($v_{rot} \approx 270 \text{km s}^{-1}$, Section 4.3). The velocity dispersion $\sigma = b/\sqrt{2} = 17 \text{km s}^{-1}$ is consistent with the vertical kinematics of a relatively thin disk.

5.2. Constraints on an outflowing wind

Galactic winds are known to be common among star-forming galaxies at $z \sim 0.5$ (Martin et al. 2012; Rubin et al. 2014), so it is worthwhile to consider whether the absorption we observe could be associated with an outflowing wind. Estimates of the half-opening angle for winds range from $\theta_w \approx 30^\circ$ for nearby galaxies like M82 and NGC 253 (Heckman et al. 1990; Westmoquette et al. 2011) to $\theta_w \approx 40^\circ\text{--}60^\circ$ for larger samples of star-forming galaxies at $z = 0.1\text{--}1$ (Chen et al. 2010c; Bordoloi et al. 2011; Kacprzak et al. 2012; Martin et al. 2012; Rubin et al. 2014). In addition, Martin et al. (2012) find that the opening angle may depend on velocity, such that higher velocity outflows tend to be more collimated, while Rubin et al. (2014) find evidence that galaxies with larger star-formation rate surface densities (Σ_{SFR}) tend to have larger wind opening angles.

As discussed in Section 4.4, only a small range of wind opening angles $51^\circ < \theta_w < 52^\circ$ could intersect our light of sight without producing a broader range of line-of-sight velocities than is observed. Furthermore, this would require a very fortunate geometry (i.e., the background source would have to be almost exactly at the edge of the outflow cone), and it would also require a large opening angle for a $|v_w| > 300 \text{km s}^{-1}$ outflow. In particular, the minimum opening angle $\theta_w = 51^\circ$ would require an outflow velocity $v_w \approx -320 \text{km s}^{-1}$ ($v_w \approx -580 \text{km s}^{-1}$) to explain the lowest (highest) velocity component we observe. Furthermore, the maximum opening angle $\theta_w = 52^\circ$ would require $v_w \approx -460 \text{km s}^{-1}$ to reproduce both the low-velocity and high-velocity components. While there is evidence that galaxies with high Σ_{SFR} values can produce large-scale, high-velocity outflows (e.g., Heckman et al. 2011; Diamond-Stanic et al. 2012; Law et al. 2012; Sell et al. 2014), the foreground galaxy has $\Sigma_{\text{SFR}} = \text{SFR}/(2\pi r_e^2) = 0.01 \mathcal{M}_\odot \text{yr}^{-1}$. This is an order of magnitude below the canonical threshold for driving winds ($\Sigma_{\text{SFR}} \geq 0.1 \mathcal{M}_\odot \text{yr}^{-1}$; Heckman 2002) and is approximately equal to the smallest Σ_{SFR} value among $z \sim 0.5$ galaxies that have been targeted in absorption-line studies of galactic winds (e.g., Kornei et al. 2012; Rubin et al. 2014). While it is clear that large-scale galactic winds are capable of producing strong Mg II absorption over a wide range of azimuthal angles around star-forming galaxies with high Σ_{SFR} values (e.g., Lundgren et al. 2012; Rubin et al. 2014), it is unlikely that the absorption lines we observe around this low- Σ_{SFR} galaxy

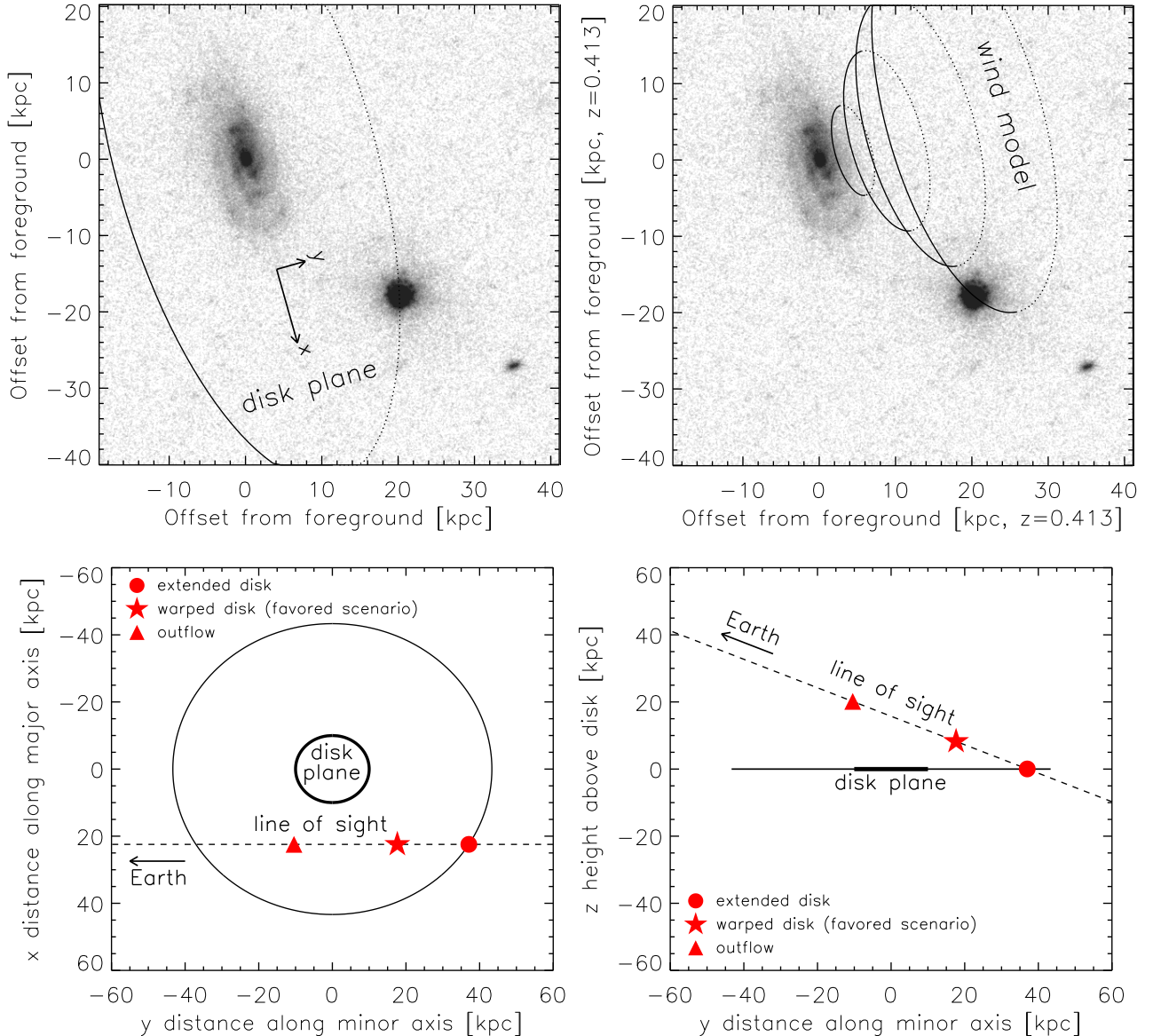


FIG. 5.— *Top Left*: Visualization of the disk plane projected on the plane of the sky. The solid and dotted lines show a circular $r = 43$ kpc disk in the same plane as the stellar disk. The x and y arrows indicate a coordinate system with x values measured along the major axis and y values measured along the minor axis. *Top Right*: Visualization of a wind model with opening angle $\theta_w = 51^\circ$ projected on the plane of the sky. The solid and dotted lines correspond to locations in the outflow cone with z heights of above the disk plane of 5 kpc, 10 kpc, 15 kpc, and 21 kpc. In this model the line of sight would intersect the edge of the outflow cone at $z = 21$ kpc. *Bottom Left*: A face-on view of the disk plane with an $r = 10$ kpc black circle that represents the stellar disk, an $r = 43$ kpc black circle that represents an extended disk, and a dashed line that represents the line of sight. The red points correspond to three potential scenarios that could explain the strongest absorption component at $v = -195$ km s $^{-1}$. The red circle corresponds to an extended disk in the same plane as the stellar disk (Section 4.2). The red star corresponds to a warped disk that is consistent with a flat rotation curve (Section 4.3). The red triangle corresponds to the edge of an outflow cone that could intersect the line of sight (Section 4.4). *Bottom Right*: An edge-on view of the disk plane with the same components as the left panel. The $r = 10$ kpc is drawn somewhat thicker than the $r = 43$ kpc disk for visualization purposes. The z height is defined relative to the plane defined by the stellar disk.

are associated with an outflowing wind.

5.3. Galactic fountains and recycled accretion

The fact that we are tracing circumgalactic gas via Mg II and Fe II absorption lines indicates that this gas must have been enriched by previous generations of supernovae (i.e., it is not pristine, metal-free gas). It is therefore worth considering models of a galactic fountain, which describes the kinematics of supernova-driven gas flows that eventually return to the disk (e.g., Breg-

man 1980; Collins et al. 2002; Fraternali & Binney 2006), and models of recycled accretion in cosmological simulations, which suggest that gas infall at $z < 1$ is dominated by material that was previously ejected in a wind (e.g., Oppenheimer et al. 2010; Ford et al. 2014).

The Bregman (1980) galactic fountain model describes how hot gas moving vertically upward and radially outward would condense via thermal instabilities into clouds that subsequently fall back towards the disk. If no external torques were applied to the gas, the orbital angu-

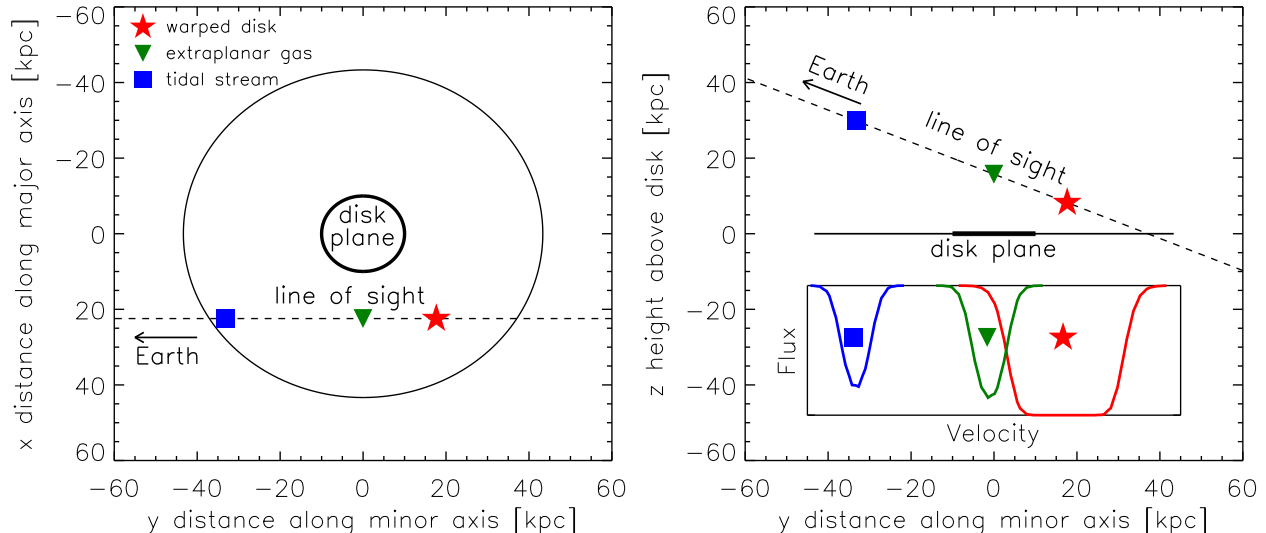


FIG. 6.— Similar to Figure 5, the left and right panels show face-on and edge-on views of the disk plane. The colored points correspond to physical scenarios that could explain each of the observed velocity components. The red star corresponds to a warped disk, which provides the best explanation for the strongest component at $v = -195 \text{ km s}^{-1}$ (Section 5.1). The green triangle corresponds to co-rotating gas near the disk-halo interface that could explain the component at $v = -256 \text{ km s}^{-1}$ (Section 5.5). The blue square corresponds to the potential location of a tidal stream that could explain the component at $v = -363 \text{ km s}^{-1}$ (Section 5.5). The inset in the right panel illustrates these three absorption components in velocity space.

lar momentum would be conserved such that gas clouds would follow a ballistic orbit before returning to the disk near the radius where the gas originated. In the context of this paper, such a model would not be able to explain the large specific angular momentum we observe at $r \approx 30 \text{ kpc}$. In other words, the rotational velocity of supernova-heated gas originating from $r \leq 5 \text{ kpc}$ would decrease by a factor of six as it traveled radially outwards (e.g., decreasing from $v_{rot} = 270 \text{ km s}^{-1}$ at $r = 5 \text{ kpc}$ to $v_{rot} = 45 \text{ km s}^{-1}$ at $r = 30 \text{ kpc}$). In contrast, the rotational velocities we infer at $r \approx 30 \text{ kpc}$ are comparable to the rotational velocities at $r \approx 5 \text{ kpc}$. Thus it is clear that a galactic fountain model in which the angular momentum of ejected gas is conserved would be inconsistent with our observations.

While the expectations for gas kinematics based on purely ballistic orbits are well understood (e.g., Collins et al. 2002; Fraternali & Binney 2006), the angular momentum of gas in a galactic fountain can also be modified by hydrodynamic interactions with the gaseous halo. For example, several authors have suggested that the drag associated with motion through the halo would absorb angular momentum from the fountain gas (e.g., Fraternali & Binney 2008; Melioli et al. 2008; Marinacci et al. 2011). This effect would increase the tension between model predictions and our observations of high specific angular momentum. On the other hand, some models have suggested that rapidly spinning halos could impart angular momentum to ejected gas (e.g., Brook et al. 2012). Furthermore, models of outflows and inflows in some cosmological simulations suggest that most of the Mg II gas in galaxy halos is associated with recycled accretion (e.g., Ford et al. 2014). In that sense, we cannot rule out the possibility that the gas we observe at $r \approx 30 \text{ kpc}$ could have previously been ejected in a wind. That said, it is unclear whether the specific angular momentum of ejected gas could be increased by a

factor of six to match our observations. A more definitive answer would require better understanding of the kinematics of hot halo gas and its hydrodynamic interactions with ejected gas (e.g., Barnabè et al. 2006).

5.4. Comparison to models of cold-mode accretion

While there is still debate about the fraction of gas accretion onto galaxies that is shock heated to the virial temperature of the halo (e.g., White & Frenk 1991; Kereš et al. 2005; Nelson et al. 2013), cosmological hydrodynamic simulations generically predict that there should be significant infall of 10^4 – 10^5 K gas onto galaxies, particularly for halo masses $M_h \leq 10^{12} M_\odot$. The filamentary structures that provide gas to Milky Way-mass galaxies at $z \leq 1$ are expected to be less dense than filaments at $z \geq 2$ and less likely to survive the journey inwards from the virial radius to the outskirts of the galactic disk (e.g., Kereš et al. 2009). Nevertheless, some simulations suggest that a fraction of the infalling cool gas at $z \leq 1$ may reach the outer disk and bring with it a significant amount of angular momentum (e.g., Roškar et al. 2010; Stewart et al. 2013; Danovich et al. 2015). As discussed in Section 5.1, the existence of warped disks in the local universe has been interpreted as evidence for cosmic infall, so it is worth considering how the kinematics we observe compare with predictions for infalling gas from zoom-in simulations.

One relevant comparison is with Stewart et al. (2011a,b), who suggest that the end of cold-mode accretion at $z \leq 1$ for $M_h \sim 10^{12} M_\odot$ halos could be observed via Mg II absorption systems that co-rotate with the galactic disk. When tracking the angular momentum of infalling gas in their simulations, they find that recently accreted cool gas has a spin parameter $\approx 4\times$ larger than that of the dark matter. In their simulations, the most recently accreted gas has the highest specific angular momentum and forms an extended, warped

disk with velocities that are offset from system by $\pm 100\text{--}300 \text{ km s}^{-1}$. The gas is expected to sink towards the center of the halo within 1–2 dynamical times (1–2 Gyr at $z \approx 1$; Stewart et al. 2013). While the interactions between outflows and inflows of hot and cool gas are not yet well understood, the properties of the cold flow disks in these simulations are broadly consistent with our observations.

5.5. Comparison with high-velocity clouds, tidal streams, and extraplanar gas

In addition to the dominant component of neutral gas in an extended disk, deep H I observations have revealed that galaxy halos in the local universe often contain $10^7\text{--}10^9 \mathcal{M}_\odot$ of neutral gas (e.g., Boomsma et al. 2005; Oosterloo et al. 2007; Sancisi et al. 2008). This extraplanar halo gas has been characterized in the Milky Way through the study of high-velocity clouds (HVCs; e.g., Wakker & van Woerden 1997; Putman et al. 2012), which trace $M_{\text{H I}} \approx 3 \times 10^8 \mathcal{M}_\odot$ of neutral gas associated with the Magellanic Stream, Leading Arm, and Magellanic Bridge, plus an additional $M_{\text{H I}} \approx 3 \times 10^7 \mathcal{M}_\odot$ distributed across the entire sky (e.g., Putman et al. 2012). The typical mass of an HVC complex is $M_{\text{H I}} = 10^5\text{--}10^6 \mathcal{M}_\odot$ (Wakker & van Woerden 1997; Putman et al. 2012), and cloud complexes as small as $M_{\text{H I}} \approx 10^5$ have been found in deep H I observations of M31 (e.g., Thilker et al. 2004; Westmeier et al. 2007).

The most prominent gaseous feature in the halo of the Milky Way is the Magellanic Stream (e.g., Wannier & Wrixon 1972; Mathewson et al. 1974), which extends more than 100° across the sky and contains more than $10^8 \mathcal{M}_\odot$ of neutral gas (e.g., Putman et al. 2003; Nidever et al. 2010). The velocity offset between the Magellanic System and the Milky Way ($v_{\text{LMC}} \approx 380 \text{ km s}^{-1}$; Kallivayalil et al. 2006) is comparable to what we observe for the optically thin component at $v_{\text{los}} = -363 \text{ km s}^{-1}$. In addition to this systemic velocity offset, the Fe II column density and velocity width we find are comparable to the observed properties of Fe II absorbers in the Magellanic Stream (e.g., Fox et al. 2010). In that sense, the data are consistent with this high-velocity component being associated with a Magellanic Stream-like structure in the halo of the foreground galaxy. We visualize the potential location of such a stream in Figure 6 with a blue square that is $d = 50 \text{ kpc}$ away from the center of the foreground galaxy, approximately equal to the distance between the Milky Way and the Large Magellanic Cloud (e.g., Freedman & Madore 2010).

The extraplanar halo gas observed within $\Delta z \sim 10 \text{ kpc}$ of nearby disk galaxies often shows evidence for co-rotation with the thin disk, and there is evidence that gas at larger z heights above the disk tends to rotate more slowly (e.g., Rand 1997; Swaters et al. 1997; Fraternali et al. 2002). This extraplanar component that has a connection to disk rotation is sometimes called “disk-halo” gas (e.g., Putman et al. 2012). In the context of this paper, it is conceivable that the optically thin absorber at $v_{\text{los}} = -256 \text{ km s}^{-1}$ could be tracing an extraplanar gas cloud with kinematics dominated by rotation. For example, locations near $|\mathbf{L}| = 40 \text{ kpc}$ ($z = 16 \text{ kpc}$, $r = 27 \text{ kpc}$) have $v_{\text{rot}}/v_{\text{los}} \leq 1.1$, implying that this velocity component could have a rotational velocity as

small as $v_{\text{rot}} \approx 270 \text{ km s}^{-1}$, which would be consistent with the disk rotational velocity. This location is marked with a green triangle in Figure 6. Such a configuration would imply essentially no change in v_{rot} with z height up to $\Delta z \approx 8 \text{ kpc}$ above the warped disk, which would be in contrast with the $\approx 15 \text{ km s}^{-1} \text{ kpc}^{-1}$ decrease in rotation velocity with z height for nearby galaxies like NGC 891 (e.g., Heald et al. 2006). That said, the precise location of this cloud along the line of sight cannot be uniquely determined from the existing data, so it is not possible to draw definitive conclusions about the vertical structure of co-rotating halo gas. Nevertheless, this intermediate-velocity absorber does exhibit the general characteristics of a co-rotating extraplanar cloud near the disk-halo interface.

5.6. Constraints on cloud sizes

The fact that we are observing gas in absorption towards an extended background source provides an important constraint on the transverse size of the absorbing clouds. Previous studies have estimated clouds sizes based on photoionization modeling (e.g., Rigby et al. 2002; Simcoe et al. 2006) and based on differences between spectra of multiply lensed quasars (e.g., Rauch et al. 1999; Petitjean et al. 2000). These studies often find cloud sizes $l = N_{\text{H}}/n_{\text{H}} \approx 100 \text{ pc}$ (e.g., Schaye et al. 2007; Prochaska & Hennawi 2009; Crighton et al. 2015) although sizes estimates as small as $l \sim 10 \text{ pc}$ (e.g., Rauch et al. 1999; Rigby et al. 2002) and as large as $l = 1\text{--}10 \text{ kpc}$ (e.g., Stocke et al. 2013; Lehner et al. 2013; Werk et al. 2014) are not uncommon.

All three velocity components we observe are well fit by models with unity covering fraction, implying that the absorbing clouds cover the entire background source. This is clear for the strong, saturated Mg II and Fe II lines at $v = -195 \text{ km s}^{-1}$ for which there is no residual flux at line center. For the weaker components at $v = -256 \text{ km s}^{-1}$ and $v = -363 \text{ km s}^{-1}$, the depth of the Mg II $\lambda 2796$ lines ($\tau \approx 2$) approach zero, and the relative depth of the Mg II $\lambda 2803$ lines ($\tau \approx 1$) confirms that the Mg II $\lambda 2796$ lines are not highly saturated. In other words, the small residual flux at line center for Mg II $\lambda 2796$ in these weaker components is explained by a moderate column density ($N_{\text{Mg II}} \approx 10^{13} \text{ cm}^{-2}$) with unity covering factor rather than a higher column density with partial covering of the background source.

Regarding the size of the background source, we use the radius that contains 90% of the total flux (r_{90}). Based on the best-fit de Vaucouleurs profile (Diamond-Stanic et al. 2012; Geach et al. 2014), this corresponds to $r_{90} = 520 \text{ pc}$ ($r_{90}/r_{50} = 5.5$; Graham et al. 2005). Accounting for the difference in angular diameter distance between $z_{\text{bg}} = 0.712$ and $z_{\text{fg}} = 0.413$, the relevant size scale at the redshift of the foreground galaxy is $l = 390 \text{ pc}$. Using this as an estimate of the size of the absorbing clouds, we can calculate the volume density of the gas ($n_{\text{H}} = N_{\text{H}}/l$) and the cloud mass ($M_c = 4/3\pi(l/2)^3 n_{\text{H}} m_p \mu$) from the estimated column density.

$$n_{\text{H}} = 0.01 \text{ cm}^{-3} \left(\frac{N_{\text{H}}}{1.2 \times 10^{19} \text{ cm}^{-2}} \right) \left(\frac{390 \text{ pc}}{l} \right) \quad (9)$$

$$M_c = 8 \mathcal{M}_\odot \left(\frac{N_{\text{H}}}{1.2 \times 10^{19} \text{ cm}^{-2}} \right) \left(\frac{l}{390 \text{ pc}} \right)^2 \quad (10)$$

The fiducial value $N_H = 1.2 \times 10^{19} \text{ cm}^{-2}$ is for the strongest component, assuming no dust depletion and solar metallicity. In comparison, the N_H , n_H , and M_c estimates for the weaker components are smaller by a factor of 30–40. As discussed in Section 4.1, these N_H values would be larger if the gas-phase abundance of Fe II were reduced by dust depletion or sub-solar metallicity.

The most robust constraint on cloud properties associated with our analysis is the $l = 390 \text{ pc}$ lower limit on the transverse cloud size. We have assumed in equations 9 and 10 that this value for the transverse size is comparable to the absorption path length, which may or may not be accurate. Our size estimate is consistent with the range of cloud sizes found in previous studies, although there is some tension with smaller size estimates found previously for weak Mg II absorbers ($l \sim 10 \text{ pc}$; Rauch et al. 1999; Rigby et al. 2002). Our results suggest that low-ionization clouds with densities as small as $n_H = 3 \times 10^{-4} \text{ cm}^{-3}$ and masses as small as $M_c = 0.2 M_\odot$ can survive in galaxy halos at distances $r = 30\text{--}50 \text{ kpc}$.

5.7. Implications for the geometry and kinematics of circumgalactic gas

A number of previous studies have combined high-resolution spectroscopy of background sources with low-resolution spectroscopy of foreground galaxies to test kinematic models of extended disks, inflows, and outflows (e.g., Steidel et al. 2002; Kacprzak et al. 2010; Bouché et al. 2013; Burchett et al. 2013; Chen et al. 2014). There are clear examples where individual absorption components can be associated with an extended disk (e.g., Steidel et al. 2002; Kacprzak et al. 2010, 2011b), but pure disk models can rarely explain all of the absorption components. This is consistent with earlier work on the kinematics of Mg II absorbers, which found that the data could be described by a combination of stronger “disk” and weaker “halo” components (e.g., Briggs et al. 1985; Lanzetta & Bowen 1992; Charlton & Churchill 1998).

In this paper, we build on this previous work by expanding the modeling to include warped disks, which are known to be ubiquitous among disk galaxies in the local universe. The existence of warps has implications for estimates of the galactocentric distance and three-dimensional kinematics associated with extended disks, and for the range of azimuthal angles over which disk-related absorption could be detected. In addition, we show how individual absorption components that are not associated with an extended disk can be associated with other structures that are known to exist in galaxy halos, including extraplanar gas and tidal streams. Furthermore, we demonstrate how this science can be done using background galaxies rather than background quasars, which provides complementary information about the sizes, densities, and masses of the absorbing components.

6. SUMMARY

We have used high-resolution spectroscopy of an extended background source to study the circumgalactic gas associated with a Milky Way–like galaxy at $z = 0.413$. We find evidence for an $r \approx 30 \text{ kpc}$ warped disk that follows the rotation curve of the foreground galaxy, consistent with observations of extended H I disks in the local universe (see Figure 4, Sections 4.3, Section 5.1). In the context of theoretical models, this gas could be associated with recycled accretion that has acquired a significant amount of angular momentum since being ejected $> 1 \text{ Gyr}$ ago (Section 5.3), and it is also consistent with predictions for infalling cool gas that co-rotates with the galactic disk (Section 5.4). In principle, a large-scale galactic wind with half-opening angle $\theta_w \approx 50^\circ$ and $v_w \approx 500 \text{ km s}^{-1}$ could reproduce similar line-of-sight kinematics, but the low Σ_{SFR} for the galaxy and the narrow line-of-sight velocity range for the absorbers suggest that this is unlikely (see Sections 4.4, 5.2). We also detect two weak Mg II absorbers whose kinematics are consistent with being associated with a tidal stream and co-rotating extraplanar gas (see Section 5.5, Figure 6). The extended nature of the background source allows us to place a lower limit on the transverse size of the absorbing clouds ($l > 0.4 \text{ kpc}$), which is broadly consistent with previous estimates in the literature.

We acknowledge useful discussions with and assistance from James Aird, James Bullock, John Chisholm, Jay Gallagher, Dušan Kereš, Britt Lundgren, Xavier Prochaska, Marc Rafelski, Kate Rubin, Jonathan Whitmore, and Art Wolfe. AMD acknowledges support from The Grainger Foundation and from the Southern California Center for Galaxy Evolution, a multi-campus research program funded by the University of California Office of Research. ALC acknowledges support from NSF CAREER award AST-1055081. RCH acknowledges support from an Alfred P. Sloan Research Fellowship and a Dartmouth Class of 1962 Faculty Fellowship. Support for HST-GO-12272 was provided by NASA through a grant from STScI. Support for Spitzer-GO-60145 was provided by contract 1419615 from JPL/Caltech. Some of the data presented herein were obtained at the W.M. Keck Observatory, which is operated as a scientific partnership among the California Institute of Technology, the University of California and the National Aeronautics and Space Administration. The Observatory was made possible by the generous financial support of the W. M. Keck Foundation. The authors wish to recognize and acknowledge the very significant cultural role and reverence that the summit of Mauna Kea has always had within the indigenous Hawaiian community. We are most fortunate to have the opportunity to conduct observations from this mountain.

REFERENCES

- Abazajian, K. N., Adelman-McCarthy, J. K., Agüeros, M. A., et al. 2009, *ApJS*, 182, 543
 Adelberger, K. L., Shapley, A. E., Steidel, C. C., et al. 2005, *ApJ*, 629, 636
 Agertz, O., Moore, B., Stadel, J., et al. 2007, *MNRAS*, 380, 963
 Barger, A. J., Cowie, L. L., & Wang, W.-H. 2008, *ApJ*, 689, 687
 Barnes, E. I., & Sellwood, J. A. 2003, *AJ*, 125, 1164
 Barnabè, M., Ciotti, L., Fraternali, F., & Sancisi, R. 2006, *A&A*, 446, 61
 Bell, E. F., McIntosh, D. H., Katz, N., & Weinberg, M. D. 2003, *ApJS*, 149, 289
 Benson, A. J., Bower, R. G., Frenk, C. S., et al. 2003, *ApJ*, 599, 38
 Bergeron, J., & Boissé, P. 1991, *A&A*, 243, 344

- Besla, G., Kallivayalil, N., Hernquist, L., et al. 2012, *MNRAS*, 421, 2109
- Bland, J., & Tully, B. 1988, *Nature*, 334, 43
- Blanton, M. R., & Roweis, S. 2007, *AJ*, 133, 734
- Boomsma, R., Oosterloo, T. A., Fraternali, F., van der Hulst, J. M., & Sancisi, R. 2005, *A&A*, 431, 65
- Bordoloi, R., Lilly, S. J., Knobel, C., et al. 2011, *ApJ*, 743, 10
- Bosma, A. 1991, *Warped Disks and Inclined Rings around Galaxies*, 181
- Bouché, N., Murphy, M. T., Péroux, C., Csabai, I., & Wild, V. 2006, *MNRAS*, 371, 495
- Bouché, N., Hohensee, W., Vargas, R., et al. 2012, *MNRAS*, 426, 801
- Bouché, N., Murphy, M. T., Kacprzak, G. G., et al. 2013, *Science*, 341, 50
- Bottema, R. 1996, *A&A*, 306, 345
- Bregman, J. N. 1980, *ApJ*, 236, 577
- Briggs, F. H., Wolfe, A. M., Turnshek, D. A., & Schaeffer, J. 1985, *ApJ*, 293, 387
- Broeils, A. H., & Rhee, M.-H. 1997, *A&A*, 324, 877
- Brook, C. B., Stinson, G., Gibson, B. K., et al. 2012, *MNRAS*, 419, 771
- Burchett, J. N., Tripp, T. M., Werk, J. K., et al. 2013, *ApJ*, 779, L17
- Chabrier, G. 2003, *PASP*, 115, 763
- Charlot, S., & Fall, S. M. 2000, *ApJ*, 539, 718
- Charlton, J. C., & Churchill, C. W. 1998, *ApJ*, 499, 181
- Chen, H.-W., Kennicutt, R. C., Jr., & Rauch, M. 2005, *ApJ*, 620, 703
- Chen, H.-W., Helsby, J. E., Gauthier, J.-R., et al. 2010, *ApJ*, 714, 1521
- Chen, H.-W., Wild, V., Tinker, J. L., Gauthier, J.-R., Helsby, J. E., Shectman, S. A., & Thompson, I. B. 2010, *ApJ*, 724, L176
- Chen, H.-W., Gauthier, J.-R., Sharon, K., et al. 2014, *MNRAS*, 438, 1435
- Chen, Y.-M., Tremonti, C. A., Heckman, T. M., Kauffmann, G., Weiner, B. J., Brinchmann, J., & Wang, J. 2010, *AJ*, 140, 445
- Churchill, C. W., Steidel, C. C., & Vogt, S. S. 1996, *ApJ*, 471, 164
- Coil, A. L., Blanton, M. R., Burles, S. M., et al. 2011, *ApJ*, 741, 8
- Collins, J. A., Benjamin, R. A., & Rand, R. J. 2002, *ApJ*, 578, 98
- Combes, F., García-Burillo, S., Braine, J., et al. 2013, *A&A*, 550, AA41
- Conroy, C., Gunn, J. E., & White, M. 2009, *ApJ*, 699, 486
- Conroy, C., & Gunn, J. E. 2010, *ApJ*, 712, 833
- Cool, R. J., Moustakas, J., Blanton, M. R., et al. 2013, *ApJ*, 767, 118
- Crighton, N. H. M., Hennawi, J. F., Simcoe, R. A., et al. 2015, *MNRAS*, 446, 18
- Croton, D. J., et al. 2006, *MNRAS*, 365, 11
- Danovich, M., Dekel, A., Hahn, O., Ceverino, D., & Primack, J. 2015, *MNRAS*, 449, 2087
- Dekel, A., & Birnboim, Y. 2006, *MNRAS*, 368, 2
- Diamond-Stanic, A. M., Moustakas, J., Tremonti, C. A., et al. 2012, *ApJ*, 755, L26
- Draine, B. T. 2011, *Physics of the Interstellar and Intergalactic Medium* (Princeton, NJ: Princeton Univ. Press)
- Erb, D. K., Quider, A. M., Henry, A. L., & Martin, C. L. 2012, *ApJ*, 759, 26
- Faucher-Giguère, C.-A., Kereš, D., & Ma, C.-P. 2011, *MNRAS*, 417, 2982
- Fazio, G. G., Hora, J. L., Allen, L. E., et al. 2004, *ApJS*, 154, 10
- Ford, A. B., Davé, R., Oppenheimer, B. D., et al. 2014, *MNRAS*, 444, 1260
- Fox, A. J., Wakker, B. P., Smoker, J. V., et al. 2010, *ApJ*, 718, 1046
- Fraternali, F., van Moorsel, G., Sancisi, R., & Oosterloo, T. 2002, *AJ*, 123, 3124
- Fraternali, F., & Binney, J. J. 2006, *MNRAS*, 366, 449
- Fraternali, F., & Binney, J. J. 2008, *MNRAS*, 386, 935
- Freedman, W. L., & Madore, B. F. 2010, *ARA&A*, 48, 673
- Fumagalli, M., Prochaska, J. X., Kasen, D., et al. 2011, *MNRAS*, 418, 1796
- Gabor, J. M., Davé, R., Oppenheimer, B. D., & Finlator, K. 2011, *MNRAS*, 417, 2676
- García-Ruiz, I., Sancisi, R., & Kuijken, K. 2002, *A&A*, 394, 769
- Gauthier, J.-R., Chen, H.-W., & Tinker, J. L. 2009, *ApJ*, 702, 50
- Gauthier, J.-R., & Chen, H.-W. 2012, *MNRAS*, 424, 1952
- Geach, J. E., Hickox, R. C., Diamond-Stanic, A. M., et al. 2014, *Nature*, 516, 68
- Graham, A. W., Driver, S. P., Petrosian, V., et al. 2005, *AJ*, 130, 1535
- Heald, G. H., Rand, R. J., Benjamin, R. A., & Bershad, M. A. 2006, *ApJ*, 647, 1018
- Heckman, T. M., Armus, L., & Miley, G. K. 1990, *ApJS*, 74, 833
- Heckman, T. M., Lehnert, M. D., Strickland, D. K., & Armus, L. 2000, *ApJS*, 129, 493
- Heckman, T. M. 2002, *Extragalactic Gas at Low Redshift*, 254, 292
- Heckman, T. M., Borthakur, S., Overzier, R., et al. 2011, *ApJ*, 730, 5
- Hopkins, P. F., Kereš, D., Oñorbe, J., et al. 2014, *MNRAS*, 445, 581
- Jenkins, E. B. 2009, *ApJ*, 700, 1299
- Jiang, I.-G., & Binney, J. 1999, *MNRAS*, 303, L7
- Joung, M. R., Putman, M. E., Bryan, G. L., Fernández, X., & Peek, J. E. G. 2012, *ApJ*, 759, 137
- Kacprzak, G. G., Churchill, C. W., Ceverino, D., Steidel, C. C., Klypin, A., & Murphy, M. T. 2010, *ApJ*, 711, 533
- Kacprzak, G. G., Churchill, C. W., Barton, E. J., & Cooke, J. 2011, *ApJ*, 733, 105
- Kacprzak, G. G., Churchill, C. W., Evans, J. L., Murphy, M. T., & Steidel, C. C. 2011, *MNRAS*, 416, 3118
- Kacprzak, G. G., Churchill, C. W., & Nielsen, N. M. 2012, *ApJ*, 760, L7
- Kacprzak, G. G., Cooke, J., Churchill, C. W., Ryan-Weber, E. V., & Nielsen, N. M. 2013, *ApJ*, 777, L11
- Kallivayalil, N., van der Marel, R. P., Alcock, C., et al. 2006, *ApJ*, 638, 772
- Kaufmann, T., Bullock, J. S., Maller, A. H., Fang, T., & Wadsley, J. 2009, *MNRAS*, 396, 191
- Kereš, D., Katz, N., Weinberg, D. H., & Davé, R. 2005, *MNRAS*, 363, 2
- Kereš, D., Katz, N., Fardal, M., Davé, R., & Weinberg, D. H. 2009, *MNRAS*, 395, 160
- Kereš, D., & Hernquist, L. 2009, *ApJ*, 700, L1
- Kornei, K. A., Shapley, A. E., Martin, C. L., et al. 2012, *ApJ*, 758, 135
- Lanzetta, K. M., & Bowen, D. V. 1992, *ApJ*, 391, 48
- Law, D. R., Steidel, C. C., Shapley, A. E., et al. 2012, *ApJ*, 759, 29
- Lehner, N., Howk, J. C., Tripp, T. M., et al. 2013, *ApJ*, 770, 138
- Lundgren, B. F., Brunner, R. J., York, D. G., et al. 2009, *ApJ*, 698, 819
- Lundgren, B. F., Brammer, G., van Dokkum, P., et al. 2012, *ApJ*, 760, 49
- Maller, A. H., & Bullock, J. S. 2004, *MNRAS*, 355, 694
- Makovoz, D., & Marleau, F. R. 2005, *PASP*, 117, 1113
- Marinacci, F., Fraternali, F., Nipoti, C., et al. 2011, *MNRAS*, 415, 1534
- Martin, C. L., Shapley, A. E., Coil, A. L., et al. 2012, *ApJ*, 760, 127
- Mathewson, D. S., Cleary, M. N., & Murray, J. D. 1974, *ApJ*, 190, 291
- McGaugh, S. S., Schombert, J. M., Bothun, G. D., & de Blok, W. J. G. 2000, *ApJ*, 533, L99
- Melioli, C., Brighenti, F., D'Ercole, A., & de Gouveia Dal Pino, E. M. 2008, *MNRAS*, 388, 573
- Ménard, B., Wild, V., Nestor, D., et al. 2011, *MNRAS*, 417, 801
- Mendez, A. J., Coil, A. L., Lotz, J., et al. 2011, *ApJ*, 736, 110
- Mo, H. J., & Miralda-Escude, J. 1996, *ApJ*, 469, 589
- Moustakas, J., Coil, A. L., Aird, J., et al. 2013, *ApJ*, 767, 50
- Nelson, D., Vogelsberger, M., Genel, S., et al. 2013, *MNRAS*, 429, 3353
- Nidever, D. L., Majewski, S. R., Butler Burton, W., & Nigra, L. 2010, *ApJ*, 723, 1618
- Nielsen, N. M., Churchill, C. W., & Kacprzak, G. G. 2013, *ApJ*, 776, 115
- Noeske, K. G., Weiner, B. J., Faber, S. M., et al. 2007, *ApJ*, 660, L43
- Ohya, Y., Taniguchi, Y., Iye, M., et al. 2002, *PASJ*, 54, 891
- Oke, J. B., et al. 1995, *PASP*, 107, 375
- Oosterloo, T., Fraternali, F., & Sancisi, R. 2007, *AJ*, 134, 1019
- Oppenheimer, B. D., Davé, R., Kereš, D., et al. 2010, *MNRAS*, 406, 2325
- Ostriker, E. C., & Binney, J. J. 1989, *MNRAS*, 237, 785
- Peng, C. Y., Ho, L. C., Impey, C. D., & Rix, H.-W. 2002, *AJ*, 124, 266
- Petitjean, P., Aracil, B., Srianand, R., & Ibata, R. 2000, *A&A*, 359, 457
- Pichon, C., Pogossyan, D., Kimm, T., et al. 2011, *MNRAS*, 418, 2493
- Planck Collaboration, Ade, P. A. R., Aghanim, N., et al. 2013, *arXiv:1303.5076*
- Prochaska, J. X., & Hennawi, J. F. 2009, *ApJ*, 690, 1558
- Putman, M. E., Staveley-Smith, L., Freeman, K. C., Gibson, B. K., & Barnes, D. G. 2003, *ApJ*, 586, 170
- Putman, M. E., Peek, J. E. G., & Joung, M. R. 2012, *ARA&A*, 50, 491
- Rand, R. J. 1997, *ApJ*, 474, 129
- Rao, S. M., Turnshek, D. A., & Nestor, D. B. 2006, *ApJ*, 636, 610
- Rauch, M., Sargent, W. L. W., & Barlow, T. A. 1999, *ApJ*, 515, 500

TABLE 1
PARAMETERS OF MODEL FITS TO CIRCUMGALACTIC ABSORPTION LINES

z	v	ion	$\log N$	b	line	τ	EW	line	τ	EW	
0.412494 ± 0.000002	-194.5 ± 0.4	Mg II	14.52 ± 0.12	23.9 ± 1.2	2796.354	35.72	0.90	2803.531	17.87	0.82	
			Fe II	14.62 ± 0.05	24.2 ± 0.9	2344.213	6.86	0.58	2374.460	1.91	0.37
						2382.764	19.58	0.71	2586.650	4.59	0.58
							2600.172	15.96	0.75		
0.412206 ± 0.000004	-255.5 ± 0.8	Mg II	13.03 ± 0.04	12.7 ± 1.1	2796.354	2.17	0.24	2803.531	1.09	0.16	
			Fe II	13.13 ± 0.05	14.1 ± 1.9	2344.213	0.39	0.07	2374.460	0.11	0.02
						2382.764	1.10	0.15	2586.650	0.26	0.05
							2600.172	0.90	0.15		
0.411700 ± 0.000002	-362.9 ± 0.5	Mg II	12.89 ± 0.03	11.6 ± 0.9	2796.354	1.70	0.20	2803.531	0.85	0.12	
			Fe II	13.03 ± 0.04	8.9 ± 1.2	2344.213	0.48	0.05	2374.460	0.13	0.02
						2382.764	1.35	0.11	2586.650	0.32	0.04
							2600.172	1.10	0.11		

NOTE. — Col. (1): Redshift. Col. (2): Velocity [km s^{-1}]. Col. (3): Ion. Col. (4): Log column density [cm^{-2}]. Col. (5): Doppler parameter [km s^{-1}]. Col. (6–11): Transitions considered, along with optical depth at line center and rest-frame equivalent width [\AA] for each transition.

- Roškar, R., Debattista, V. P., Brooks, A. M., et al. 2010, MNRAS, 408, 783
- Rigby, J. R., Charlton, J. C., & Churchill, C. W. 2002, ApJ, 565, 743
- Rubin, K. H. R., Prochaska, J. X., Koo, D. C., Phillips, A. C., & Weiner, B. J. 2010, ApJ, 712, 574
- Rubin, K. H. R., Weiner, B. J., Koo, D. C., Martin, C. L., Prochaska, J. X., Coil, A. L., & Newman, J. A. 2010, ApJ, 719, 1503
- Rubin, K. H. R., Prochaska, J. X., Koo, D. C., et al. 2014, ApJ, 794, 156
- Sancisi, R. 1976, A&A, 53, 159
- Sancisi, R., Fraternali, F., Oosterloo, T., & van der Hulst, T. 2008, A&A Rev., 15, 189
- Schaye, J., Carswell, R. F., & Kim, T.-S. 2007, MNRAS, 379, 1169
- Sell, P. H., Tremonti, C. A., Hickox, R. C., et al. 2014, MNRAS, 441, 3417
- Shang, Z., Zheng, Z., Brinks, E., et al. 1998, ApJ, 504, L23
- Shapiro, P. R., & Field, G. B. 1976, ApJ, 205, 762
- Shen, J., & Sellwood, J. A. 2006, MNRAS, 370, 2
- Shopbell, P. L., & Bland-Hawthorn, J. 1998, ApJ, 493, 129
- Simcoe, R. A., Sargent, W. L. W., Rauch, M., & Becker, G. 2006, ApJ, 637, 648
- Springel, V., & Hernquist, L. 2002, MNRAS, 333, 649
- Steidel, C. C., Dickinson, M., & Persson, S. E. 1994, ApJ, 437, L75
- Steidel, C. C., Kollmeier, J. A., Shapley, A. E., Churchill, C. W., Dickinson, M., & Pettini, M. 2002, ApJ, 570, 526
- Steidel, C. C., Erb, D. K., Shapley, A. E., Pettini, M., Reddy, N., Bogosavljević, M., Rudie, G. C., & Rakic, O. 2010, ApJ, 717, 289
- Stewart, K. R., Kaufmann, T., Bullock, J. S., Barton, E. J., Maller, A. H., Diemand, J., & Wadsley, J. 2011, ApJ, 735, L1
- Stewart, K. R., Kaufmann, T., Bullock, J. S., et al. 2011, ApJ, 738, 39
- Stewart, K. R., Brooks, A. M., Bullock, J. S., et al. 2013, ApJ, 769, 74
- Stocke, J. T., Keeney, B. A., Danforth, C. W., et al. 2013, ApJ, 763, 148
- Swaters, R. A., Sancisi, R., & van der Hulst, J. M. 1997, ApJ, 491, 140
- Thilker, D. A., Braun, R., Walterbos, R. A. M., et al. 2004, ApJ, 601, L39
- Tremonti, C. A., Moustakas, J., & Diamond-Stanic, A. M. 2007, ApJ, 663, L77
- Tripp, T. M., Meiring, J. D., Prochaska, J. X., et al. 2011, Science, 334, 952
- van de Voort, F., Schaye, J., Booth, C. M., Haas, M. R., & Dalla Vecchia, C. 2011, MNRAS, 414, 2458
- Tully, R. B., & Fisher, J. R. 1977, A&A, 54, 661
- Veilleux, S., Cecil, G., & Bland-Hawthorn, J. 2005, ARA&A, 43, 769
- Vogt, S. S., et al. 1994, Proc. SPIE, 2198, 362
- Vogelsberger, M., Genel, S., Sijacki, D., et al. 2013, MNRAS, 436, 3031
- Wakker, B. P., & van Woerden, H. 1997, ARA&A, 35, 217
- Wannier, P., & Wrixon, G. T. 1972, ApJ, 173, L119
- Weiner, B. J., et al. 2009, ApJ, 692, 187
- Werk, J. K., Prochaska, J. X., Tumlinson, J., et al. 2014, ApJ, 792, 8
- Westmeier, T., Braun, R., Brüns, C., Kerp, J., & Thilker, D. A. 2007, New Astronomy Reviews, 51, 108
- Westmoquette, M. S., Smith, L. J., & Gallagher, J. S., III 2011, MNRAS, 414, 3719
- White, S. D. M., & Rees, M. J. 1978, MNRAS, 183, 341
- White, S. D. M., & Frenk, C. S. 1991, ApJ, 379, 52
- Willmer, C. N. A., Faber, S. M., Koo, D. C., et al. 2006, ApJ, 647, 853
- Yun, M. S. 1999, Galaxy Interactions at Low and High Redshift, 186, 81
- Zibetti, S., Ménard, B., Nestor, D. B., et al. 2007, ApJ, 658, 161